JOURNAL OF AIRCRAFT
Vol. 36, No. 4, July–August 1999

Airfoil Drag Prediction and Decomposition

D. D. Chao* and C. P. van Dam†
University of California, Davis, Davis, California 95616-5294

The accuracy and the consistency of numerical techniques for the prediction of the aerodynamic drag of airfoils in viscous transonic and subsonic flows are explored. Attention is paid to the calculation of the total drag as well as to the decomposition of the drag into its physical components: viscous drag and wave drag. Two different Reynolds-averaged Navier–Stokes solvers are used to generate the flowfield solutions for the NLF(1)-0416 and the RAE 2822 airfoils. The results show that wake integration can produce results comparable with those the often-used surface integral technique, thus demonstrating that wake integration has great potential in simplifying drag calculations for more complex problems such as multielement airfoils or complex three-dimensional configurations.

Introduction

THE aerodynamic drag of an aircraft flying at subsonic speeds can be separated into viscous (or profile) drag and induced drag. The former consists of skin friction and form drag and is generated through the action of viscosity within the boundary layer. The latter is the result of the shedding of vorticity that accompanies the production of lift. At transonic and supersonic speeds, another drag-producing mechanism arises from the radiation of energy away from the aircraft in the form of pressure waves, i.e., wave drag. Accurate prediction of the drag during the various stages of the development process of an aircraft is of importance to the efficiency of this process as well as to the economic success of the aircraft. Additionally, knowledge about the physical components of the drag is of importance to the prediction of scale effects on aircraft drag.

The most common technique to calculate the drag of an airfoil, wing, or complete configuration is based on the integration of the pressure and shear stress acting on the surface of the configuration. This so-called near-field technique can lead to inaccuracies in the drag calculation, as illustrated in Fig. 1. In Fig. 1 the surface pressure is plotted as a function of the vertical surface coordinate for a typical airfoil at incompressible conditions. From this figure it is clear that determining the form-drag contribution to the total drag from surface integration involves subtraction of a large force component in the thrust direction from a slightly larger force component in the drag direction. Thus the form drag can be successfully determined only if the pressure distribution along the surface is known with great accuracy and in great detail.[1] A standard alternative to calculating aerodynamic forces by means of surface integration is to compute the forces around a far-field surface enclosing the body, a technique known as far-field integration. The advantage of this technique is that the shear-stress contribution can be neglected if the control surface is located outside the viscous layer; however, an additional term (momentum flux) must be included in the analysis. Another alternative drag prediction method is the wake integration technique, which is based on the principle that the aerodynamic drag of a configuration is equal to the momentum deficit in the wake far downstream of the configuration. The main advantage of this technique is that no detailed information on the surface geometry of the configuration is required. It also allows for the decomposition of the drag into its physical components, i.e., viscous drag, wave drag, and induced drag. Another reason for using the drag from numerical solutions is the fact that the wake survey technique is commonly used in experiments to measure the profile drag and the induced drag of wings. Therefore, to have a consistent comparison, experimental drag obtained from wake survey should be compared with predicted drag determined from wake integration.

Both the far-field and the wake integration techniques are closely related to the surface integration technique, and all three techniques are derived from momentum integral theory. The limitations of the surface integration technique in computing drag have been known for many years. Yet it continues to be the standard drag prediction technique in computational fluid dynamics (CFD). Several recent studies have noted the need for improved reliability and accuracy in CFD drag calculations. One of the earliest studies on this subject was by Yu et al.,[2] who explored the three different drag prediction techniques for several two- and three-dimensional configurations. Slooff,[3] van der Vooren and Slooff,[4] and Lock[1,5] have published several insightful papers on CFD-based drag prediction. Recently the wake integration technique was successfully applied to the prediction of lift, induced drag, and wave drag of three-dimensional wings in subsonic and transonic flows based on CFD solutions of the Euler equations.[6,7] However, most of these studies have been limited to inviscid flows, focusing on solutions of the potential and Euler equations for two- and three-dimensional configurations. The ultimate goal is to apply the wake integration technique to numerical solutions of the three-dimensional Reynolds-averaged Navier–Stokes (RaNS) equations. In this study, the emphasis is on the interim step; the prediction of viscous drag and wave drag is based on numerical solutions of the two-dimensional RaNS equations.

The objective of this study is to compare the accuracy of the surface integration and the wake integration techniques in predicting the aerodynamic drag from computed solutions of the two-dimensional RaNS equations. In the following sections, the different drag integration techniques are derived and the numerical implementation of these techniques are discussed. The RaNS codes and the test cases used in this study are also presented. Last, the techniques are applied to determine the profile drag for several airfoils at subsonic flow conditions and the profile drag and the wave drag at transonic conditions.

Drag Prediction Methods

The fundamental formula for the total aerodynamic force acting on a configuration is derived by application of the conservation law of momentum to the control volume enclosing the entire configuration, as shown in Fig. 2. With body forces neglected, the resulting equation is

$$\int_S [\boldsymbol{T} : \boldsymbol{n} - \rho \boldsymbol{V}(\boldsymbol{V} \cdot \boldsymbol{n})]\,\mathrm{d}S = 0 \qquad (1)$$

Presented as Paper 98-2783 at the AIAA 16th Applied Aerodynamics Conference, Albuquerque, NM, 15–18 June 1998; received 17 November 1998; revision received 20 March 1999; accepted for publication 3 April 1999.

*Ph.D. Student, Department of Mechanical and Aeronautical Engineering. Student Member AIAA.

†Professor, Department of Mechanical and Aeronautical Engineering. Senior Member AIAA.

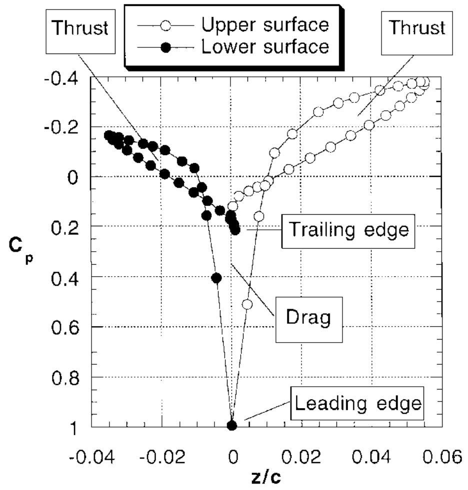

Fig. 1 Pressure distribution as a function of vertical surface coordinate for a cambered airfoil at zero angle of attack.

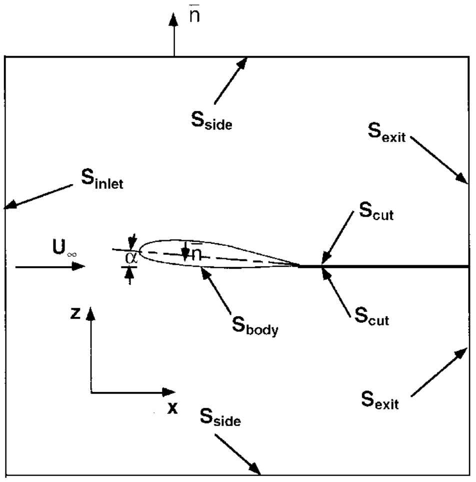

Fig. 2 Control volume used in derivation of aerodynamic forces.

where S represents the entire control surface, $\boldsymbol{n} = n_x\hat{\boldsymbol{i}} + n_y\hat{\boldsymbol{j}} + n_z\hat{\boldsymbol{k}}$ represents the outward unit vector normal to S, ρ represents the fluid density, and $\boldsymbol{V} = u\,\hat{\boldsymbol{i}} + v\hat{\boldsymbol{j}} + w\,\hat{\boldsymbol{k}}$ represents the velocity vector. The tensor product $\boldsymbol{T} : \boldsymbol{n}$ contains contributions from the pressure p and the shear stress $\boldsymbol{\tau}$,

$$\boldsymbol{T} : \boldsymbol{n} = -p\boldsymbol{n} + \boldsymbol{\tau} : \boldsymbol{n} \tag{2}$$

where the stress tensor is defined as

$$\boldsymbol{\tau} = \begin{bmatrix} \tau_{xx} & \tau_{xy} & \tau_{xz} \\ \tau_{yx} & \tau_{yy} & \tau_{yz} \\ \tau_{zx} & \tau_{zy} & \tau_{zz} \end{bmatrix} \tag{3}$$

Note that S consists of S_{far}, S_{cut}, and S_{body}, where $S_{\text{far}} = S_{\text{inlet}} + S_{\text{side}} + S_{\text{exit}}$. Consequently, Eq. (1) can be written as

$$\int_{S_{\text{far}}} [\,]\,\mathrm{d}S + \int_{S_{\text{body}}} [\,]\,\mathrm{d}S + \int_{S_{\text{cut}}} [\,]\,\mathrm{d}S = 0 \tag{4}$$

where [ ] denotes $[\boldsymbol{T} : \boldsymbol{n} - \rho\boldsymbol{V}(\boldsymbol{V}\cdot\boldsymbol{n})]$. The third integral in Eq. (4) is zero since $\boldsymbol{n}$ along the upper and lower side of the cut points in opposite directions. The momentum-flux term $\rho\boldsymbol{V}(\boldsymbol{V}\cdot\boldsymbol{n})$ in the second integral is zero in the general case of solid body surface. Thus Eq. (4) reduces to

$$\int_{S_{\text{body}}} [\boldsymbol{T} : \boldsymbol{n}]\,\mathrm{d}S = -\int_{S_{\text{far}}} [\boldsymbol{T} : \boldsymbol{n} - \rho\boldsymbol{V}(\boldsymbol{V}\cdot\boldsymbol{n})]\,\mathrm{d}S \tag{5}$$

where the integral on the left-hand side represents the total force imposed by the body on the fluid. Therefore, the aerodynamic drag, defined as the force in the freestream direction imposed by the fluid on the configuration, is

$$D = -\int_{S_{\text{body}}} [-pn_x + \tau_{xx}n_x + \tau_{xy}n_y + \tau_{xz}n_z]\,\mathrm{d}S \tag{6}$$

or

$$D = \int_{S_{\text{far}}} [-pn_x + \tau_{xx}n_x + \tau_{xy}n_y + \tau_{xz}n_z - \rho u(\boldsymbol{V}\cdot\boldsymbol{n})]\,\mathrm{d}S \tag{7}$$

where the freestream velocity vector is aligned with the x axis (Fig. 2). Equations (6) and (7) represent the surface and far-field expressions for the drag, respectively. To correct for any mass conservation error in the flowfield, the far-field expression can be evaluated as follows:

$$D = \int_{S_{\text{far}}} [-pn_x + \tau_{xx}n_x + \tau_{xy}n_y + \tau_{xz}n_z - \rho(u - U_\infty)(\boldsymbol{V}\cdot\boldsymbol{n})]\,\mathrm{d}S \tag{8}$$

where U_∞ represents the freestream velocity. The wake expression for the drag can be derived from Eq. (8) by moving the inlet and side faces to infinity. The resulting wake expression is

$$D = \int_{S_{\text{exit}}} [(p_\infty - p) + \tau_{xx} - \rho u(u - U_\infty)]\,\mathrm{d}S \tag{9}$$

where S_{exit} is normal to the freestream velocity vector, which again is aligned with the x axis.

Equations (6), (8), and (9), presented here in their most general form, provide three fundamental integrals for the evaluation of the aerodynamic drag. Note that these three expressions should predict an identical drag value for a given flowfield. However, as a result of problems encountered in the numerical integration of these expressions as well as various errors contained in the numerical solutions of the flow solvers, the drag values may differ substantially.

Wave Drag

When the Euler equation formulation is used, wave drag can be related to the entropy increase across a shock through the Oswatitsch drag integral[8]:

$$D_{\text{wave}} = \frac{T_\infty}{U_\infty}\int_S (s - s_\infty)\rho(\boldsymbol{V}\cdot\boldsymbol{n})\,\mathrm{d}S \tag{10}$$

where

$$s - s_\infty = \frac{R}{\gamma - 1}\ell n\left[\frac{p/p_\infty}{(\rho/\rho_\infty)^\gamma}\right]$$

represents the specific entropy produced by shocks, R is the gas constant, γ is the specific heat ratio, and T_∞ is the freestream temperature. A variation of the expression for the wave drag is derived by van Dam et al.[7]:

$$D_{\text{wave}} = \frac{p_\infty}{R}\int_{S_{\text{exit}}} (s - s_\infty)\,\mathrm{d}S \tag{11}$$

In viscous flows, the drag integral, Eq. (11), represents the entire profile drag, i.e., wave drag and viscous drag. Therefore Eq. (11) should be evaluated across the shocks to obtain only the wave drag.

Numerical Implementation

A postprocessing computer code incorporating the three different integrals has been developed to compute drag from numerical solutions of the RaNS equations. The flowfield solution file in standard PLOT3D (Ref. 9) format is generated for a given configuration at prescribed freestream conditions and boundary-layer transition locations by a RaNS code. For two-dimensional compressible flows, this file generally contains ρ, ρu, ρv, and the total energy e at each grid point. In addition, a file containing the turbulent eddy viscosity at each grid point is generated. Based on this flowfield information, the postprocessing code first computes the pressure and the shear stresses and then the drag coefficient $c_d = 2D'/(\rho U_\infty^2 c)$, where c is the airfoil chord, by numerically integrating one of the drag expressions. Integration of the far-field expression is performed along a user-specified grid line. Integration of the wake expression is performed along a vertical line placed at a user-specified distance downstream of the configuration. Flowfield information along this wake line is obtained by interpolation of the flowfield solution from surrounding grid points by use of bilinear interpolation. Integration points along the wake line are clustered to match closely the distribution of nearby grid points to allow for accurate transfer of flowfield information onto the wake line. Of course, this assumes that the computational grid already has enough points in the wake region and that the grid points are clustered such that the complete wake is captured. In general, a grid adaptation scheme is required for accurately resolving the wake region. However, in the course of implementing the wake integration method, it was found that a sufficient point distribution in the wake can be obtained by fanning out grid lines clustered along the appropriately curved wake cut of a C grid. Once the flowfield information is interpolated onto the wake line, the wake expression is integrated until the freestream total pressure is recovered. In general, CFD solutions for configurations at angle of attack are obtained by rotating the freestream velocity vector and keeping the configuration horizontal. However, when the three integral expressions for drag were derived, the freestream velocity vector was assumed to align with the x axis. Therefore, in this study, we computed the flowfields by rotating the configuration to the appropriate angle of incidence and keeping the freestream vector horizontal (Fig. 2).

Flow Solvers and Grid Generator

The airfoil flowfields are computed with two well-known RaNS codes: ARC2D (Ref. 10) and INS2D (Ref. 11). A brief description of each flow solver and a discussion of the grid generation technique used are presented.

ARC2D was developed by Pulliam and Steger.[10] The code solves the compressible RaNS equations in strong conservation-law form. The governing equations in generalized curvilinear coordinates are central differenced in standard second-order form and solved with the implicit Beam–Warming approximate factorization scheme.[12] Second- and fourth-order artificial dissipation terms are added for numerical stability. The code uses local time stepping and mesh sequencing to accelerate convergence. ARC2D has been extensively applied to analyze inviscid and viscous flows over airfoils.[13–15]

INS2D was developed by Rogers and Kwak.[11] The code solves the incompressible RaNS equations in generalized curvilinear coordinates by using the artificial compressibility method of Chorin[16] to couple the velocity and the pressure fields. The convective fluxes are upwind differenced by a third-order flux-difference splitting scheme developed by Roe,[17] whereas the viscous fluxes are central differenced in standard second-order form. The resulting equations are solved by implicit line-relaxation sweeps. The code can handle both multiblock patched grids as well as overset chimera grids and has been applied extensively to analyze flows over multielement airfoils.[18–20]

Turbulence Model

Several turbulence models are available in each of the two flow solvers. However, since the objective of this study was not a comparison of the different turbulence models but a comparison of drag prediction techniques, the Spalart–Allmaras model[21] was selected and used throughout this study. For this turbulence model the Reynolds stresses are given by $-u_i'u_j' = 2\nu_t S_{ij}$, where S_{ij} is the strain-rate tensor and ν_t is the eddy viscosity solved for by the model. Whereas this is a reasonable model for the $i \neq j$ terms, questions regarding the Reynolds stress prediction arise for $i = j$ terms. Note that for the high Reynolds flows considered here it is the normal stress term $-\rho u'^2$ that provides the dominant contribution to the viscous stress τ_{xx} in Eq. (9).

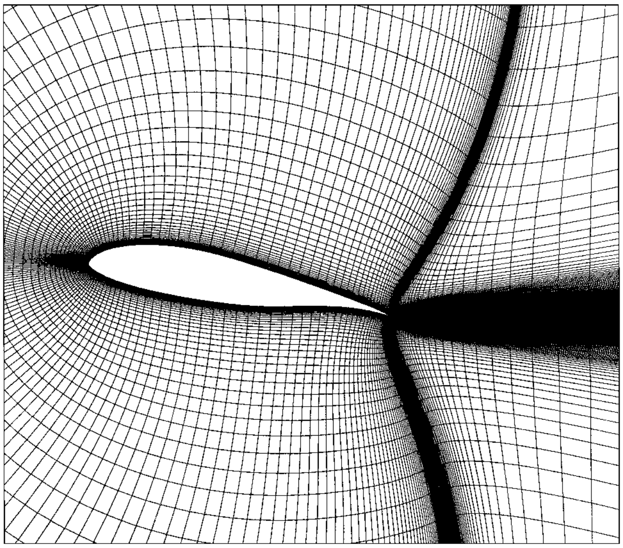

a) Complete airfoil

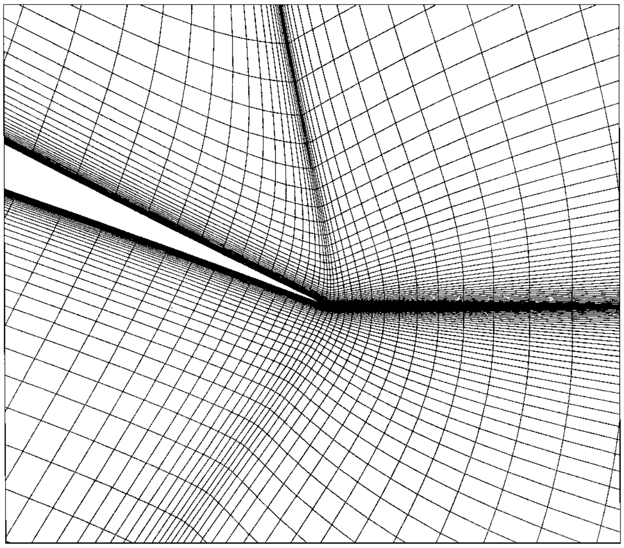

b) Trailing-edge region

Fig. 3 Close-up view of a typical grid for the NLF(1)-0416 airfoil.

Grid Generation

All computational grids used in this study are of the C type. The grids are created with the hyperbolic grid generator HYPGEN.[22] The grid spacing near the wall is kept at $y^+ < 4$ for all viscous cases. In the critical trailing-edge region the circumferential grid spacing is reduced to 1×10^{-4} of the chord. The maximum stretching ratio throughout the grid is kept below 1.2. In addition, in the wake region the circumferential wake lines are fanned out to provide adequate grid resolution. A close-up view of a typical grid is shown in Fig. 3. This particular grid is used to generate the flowfield at $\alpha = 10$ deg. Note the fanning of the grid lines in the wake region of the airfoil.

Test Cases

Two single-element airfoils are used in this drag prediction study: the low-subsonic airfoil NLF(1)-0416 (Ref. 23) and the high-subsonic airfoil RAE 2822 (Ref. 24).

The NLF(1)-0416, shown in Fig. 4, is a natural-laminar-flow airfoil designed for light airplanes to have a high maximum lift coefficient and low cruise drag. The airfoil has a maximum thickness-to-chord ratio of 16% and was tested with free and fixed transition at $M_\infty = 0.1$ and a range of Reynolds numbers in the low-turbulence pressure tunnel (LTPT) at the NASA Langley Research Center.[23] Here, we concentrate on the results obtained at $Re = 4.0 \times 10^6$ and

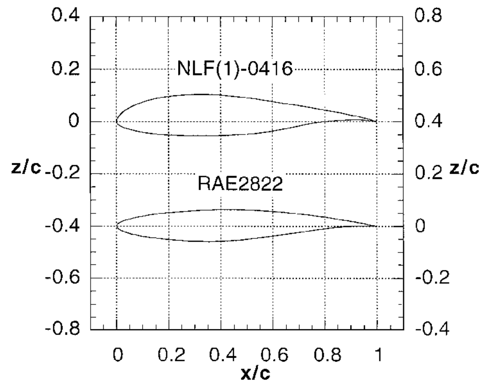

Fig. 4 Geometries of airfoils.

transition fixed at 7.5% of the chord for both upper and lower surfaces. The reported drag values are based on a wake survey taken one chord downstream of the airfoil trailing edge.

The RAE 2822, shown in Fig. 4, is an airfoil with a rear-loaded, subcritical, rooftop-type pressure distribution at its design conditions: $M_\infty = 0.66$ and $c_l = 0.56$. It has a maximum thickness ratio of 12.1% and was extensively tested in the RAE 8 × 6 ft transonic over a range of Mach numbers.[24] Here results are presented for $M_\infty = 0.676$ and $Re = 5.7 \times 10^6$ (case 1 in Ref. 24) and $M_\infty = 0.730$ and $Re = 6.5 \times 10^6$ (case 9 in Ref. 24). Transition was fixed at 11% of the chord for both upper and lower surfaces for case 1 and at 3% of the chord for both surfaces for case 9. Note that the reported drag values are based on a wake survey at a distance of one chord downstream of the airfoil trailing edge.

Results and Discussion

NLF(1)-0416

Results for this airfoil were obtained by use of both RaNS codes in which the ARC2D solutions were obtained at $M_\infty = 0.25$ to prevent low Mach number accuracy problems. Application of the recently developed version of ARC2D that includes a low Mach number preconditioning option would eliminate this problem and allow for accurate flow solutions at $M_\infty = 0.1$, which was the Mach number used to obtain the wind-tunnel results. In Fig. 5 the measured and the predicted pressure distributions at a nominal lift coefficient $c_l = 1.11$ are shown for this airfoil. The reported angle of attack at this lift coefficient is $\alpha = 6.10$ deg (Ref. 22). The angle of attack to match this c_l is $\alpha = 5.80$ deg for INS2D and $\alpha = 5.43$ deg for ARC2D. Note that the compressibility effect on the flowfield causes a slight increase in the lift-curve slope for the ARC2D solution obtained at $M_\infty = 0.25$ and consequently a slight decrease in angle of attack to match $c_l = 1.11$. The agreement between the computed and the measured pressure distributions is excellent. At this lift coefficient the measured drag coefficient $c_d = 0.0113$, whereas surface integration based on the INS2D and ARC2D solutions gives $c_d = 0.0115$ and 0.0110, respectively. With the evaluation station set at one chord downstream of the trailing edge, wake integration gives $c_d = 0.0113$ and 0.0113 based on the INS2D and ARC2D solutions, respectively. Thus both RaNS methods predict the drag well, and in both cases the drag based on wake integration is fairly consistent with the drag based on surface integration.

In Fig. 6 the predicted and the measured drag polars are compared for $Re = 4.0 \times 10^6$ and transition fixed at 0.075c. The INS2D results are shown in Fig. 6a whereas the ARC2D results are shown in Fig. 6b. Overall, the predicted values are in good agreement with the experimental data. In all cases, drag coefficients obtained from wake integration are within two drag counts ($\Delta c_d = \pm 0.0002$) of the surface-integrated values. Direct comparisons of the drag data based on INS2D- and ARC2D-generated flow fields reveal only slight differences between the two solution sets. Based on this observation, combined with the fact that INS2D is limited to incompressible flows, only results obtained with ARC2D are presented in the remainder of this study.

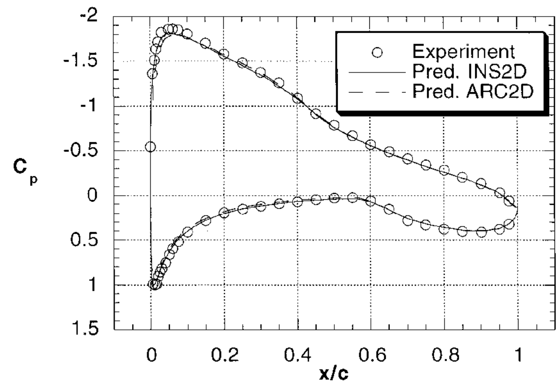

Fig. 5 Pressure distribution of NLF(1)-0416 at c_l = 1.11 and Re = 4.0 × 10^6 (α_{exp} = 6.10 deg, α_{ARC2D} = 5.43 deg, and α_{INS2D} = 5.80 deg).

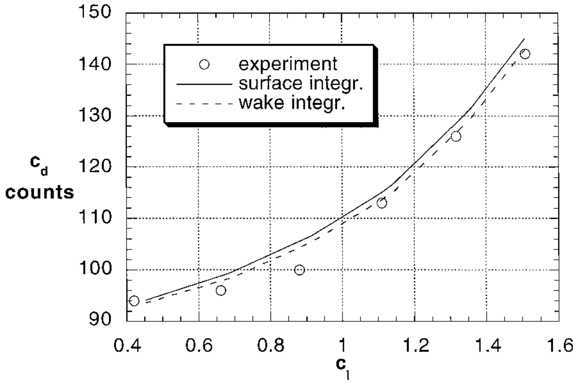

a) INS2D

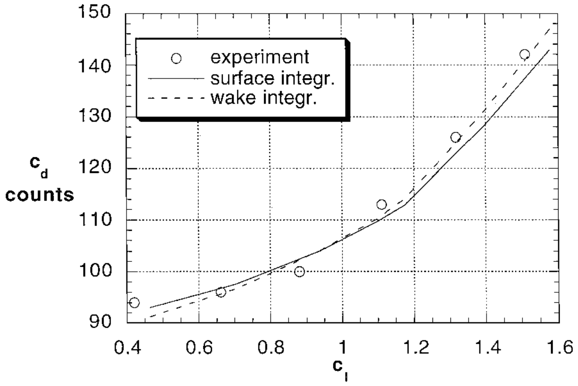

b) ARC2D

Fig. 6 Predicted and measured drag polars of NLF(1)-0416 at Re = 4.0 × 10^6.

In Fig. 7 the total wake drag and the separate contributions of the three components (pressure thrust, momentum drag, and viscous stress) are plotted as functions of the integration station. The total drag is independent of the location of the integration station (as it should be) except in the region just aft of the trailing edge. In this near-wake region, steep velocity gradients in both the normal and the streamwise directions make this region susceptible to flow modeling errors. The contribution of the viscous-stress term to the wake drag is several orders of magnitude smaller than the contribution of the pressure and the momentum terms and drops below 0.1 counts within one chord length downstream of the trailing edge. With increasing distance from the trailing edge, the (negative) contribution of the pressure term to the total drag diminishes and at approximately 10 chords only the momentum-deficit term remains and

$$c_d = 2\int_{-\infty}^{\infty} \frac{\rho u}{\rho_\infty U_\infty}\left(1 - \frac{u}{U_\infty}\right) \mathrm{d}\left(\frac{z}{c}\right) = 2\frac{\theta_\infty}{c}$$

Table 1 Comparison of drag coefficients for RAE 2822 at M_∞ = 0.676 and Re = 5.7 × 10^6 (case 1)

Parameter	Experiment	Prediction
α, deg	2.40	1.87
c_l	0.566	0.566
c_d (experimental)	0.0085	——
c_d (surface integration)	——	0.0085
c_d (wake integration)	——	0.0082

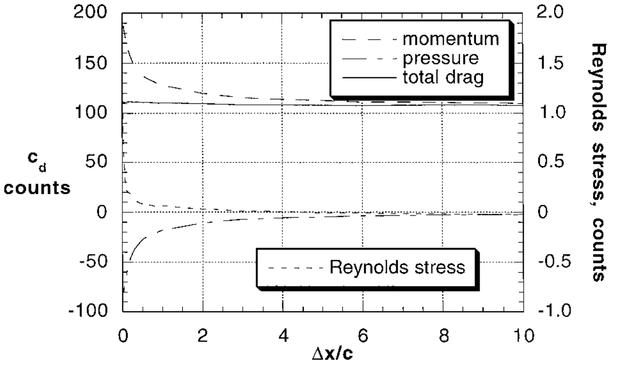

Fig. 7 Contribution of pressure, momentum-flux, and Reynolds stress terms to wake integral of NLF(1)-0416 at c_l = 1.11 and Re = 4.0 × 10^6.

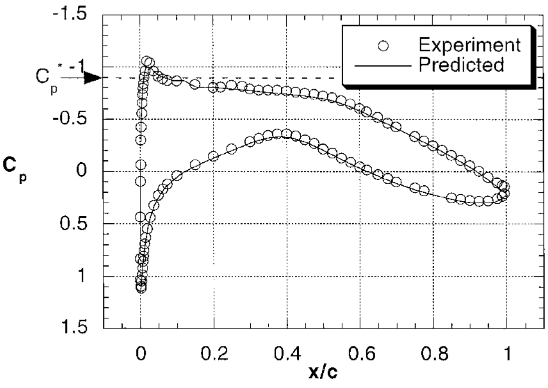

Fig. 8 Pressure distribution of RAE 2822 at c_l = 0.566, M_∞ = 0.676, and Re = 5.7 × 10^6 (case 1).

where θ_∞ represents the momentum thickness of the wake far downstream.

RAE 2822

The RAE 2822 was studied to obtain a better understanding of drag prediction at high subsonic and transonic flow conditions. In Fig. 8 the measured and the predicted pressure distributions for case 1 are shown. The reported angle of attack for this test case is 2.40 deg (Ref. 24). The airfoil was designed to have a subcritical rooftop-type pressure distribution. However, both the test Mach number $M_\infty = 0.676$ and the measured lift coefficient $c_l = 0.566$ are slightly higher than the design Mach number of 0.66 and design lift coefficient of 0.56. As a result, the measured pressure distribution reveals a very small supersonic region near the leading edge. At the test Mach number of 0.676 the critical pressure coefficient C_p^* is -0.883 whereas the measured minimum pressure coefficient is -1.05. The angle of attack used during the numerical simulation was reduced to $\alpha = 1.87$ deg in order to match the lift coefficient $c_l = 0.566$. Figure 8 shows good agreement between the measured and predicted pressure distributions.

In Table 1 the measured drag is compared with the predicted drag based on surface integration and wake integration. The wake integral is evaluated at one chord downstream of the trailing edge. The surface integration result matches the measured drag coefficient perfectly, whereas the wake integration underpredicts the drag coefficient by three counts.

Table 2 Comparison of drag coefficients for RAE 2822 at M_∞ = 0.730 and Re = 6.5 × 10^6 (case 9)

Parameter	Experiment	Prediction	Prediction (fine grid)
α, deg	3.19	2.81	2.81
c_l	0.803	0.802	0.809
c_d (experimental)	0.0168	——	——
c_d (surface integration)	——	0.0166	0.0166
c_d (wake integration)	——	0.0162	0.0162

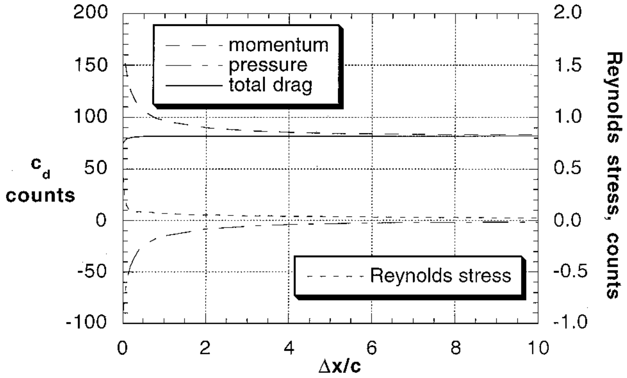

Fig. 9 Contribution of pressure, momentum-flux, and Reynolds stress terms to wake integral of RAE 2822 (case 1).

Figure 9 provides more insight into the wake integration by plotting the total drag as well as its three components (pressure thrust, momentum drag, viscous stress) as functions of the integration station. The total drag is again independent of the integration station (as it should be) except in the region just aft of the trailing edge. The viscous-stress term dies out within one chord length downstream of the trailing edge. With increasing distance the contribution of the pressure term diminishes and at approximately 10 chords only the momentum-deficit term remains.

In Ref. 24 measured wake profiles are presented at several chordwise stations. These data are presented in terms of u/U_P as a function of z/c, where u is the local velocity and U_P is the velocity obtained from a pitot pressure measurement at the edge of the shear layer and a surface pressure coefficient $(C_p)_P$ at the trailing edge. In Fig. 10 comparisons are presented of the predicted and the measured velocity profiles at the trailing edge of the airfoil ($x/c = 1.0$ or $\Delta x/c = 0$) and at 0.025 chord lengths downstream of the trailing edge ($\Delta x/c = 0.025$). Good agreement is obtained at both locations. The discrepancy in the wake-edge velocities U_P is due to the fact that the same value for $(C_p)_P = 0.145$ was applied to convert the CFD results into the form used in Ref. 24 to present the velocity profiles. The slight difference between measured and calculated surface pressures in the trailing-edge region leads to the apparent mismatch in edge velocities.

In Fig. 11 the measured and the predicted pressure distributions for case 9 (Ref. 24) are shown. The freestream Mach number is 0.730, and the measured lift coefficient is $c_l = 0.803$ at a reported angle of attack of 3.19 deg. At these conditions a strong shock occurs on the upper surface at approximately $x/c = 0.55$. To match the lift coefficient, the angle of attack used during the numerical simulation is reduced to $\alpha = 2.85$ deg. Figure 11 shows good agreement between the measured and the predicted pressure distributions.

In Table 2 the measured drag is compared with the predicted drag coefficients. Again the wake drag is based on the evaluation of the wake integral at one chord downstream of the airfoil trailing edge. For this test case the agreement between experiment and numerical simulation is not as good. The reason for this may be the slightly more forward location of the shock in the numerical simulation as compared with the measured shock location.

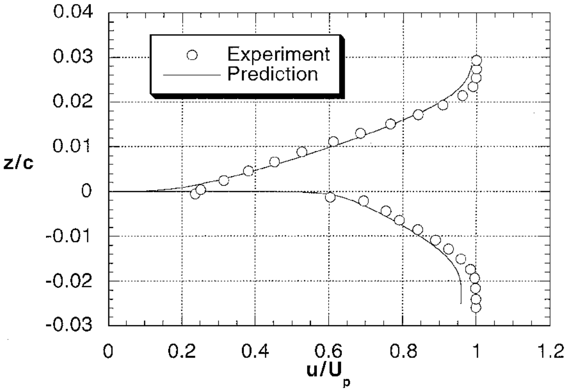

a) $\Delta x/c = 0$, $(C_p)_P = 0.145$

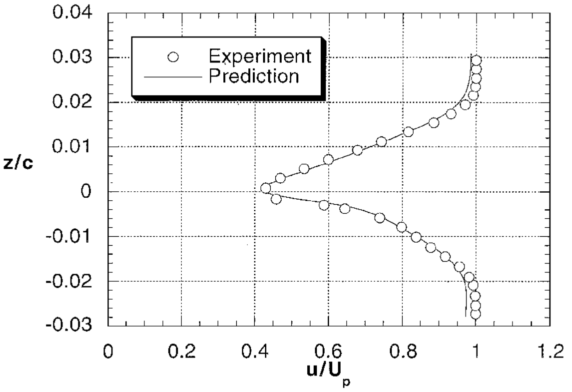

b) $\Delta x/c = 0.025$, $(C_p)_P = 0.145$

Fig. 10 Predicted and measured near-wake profiles for RAE 2822 (case 1).

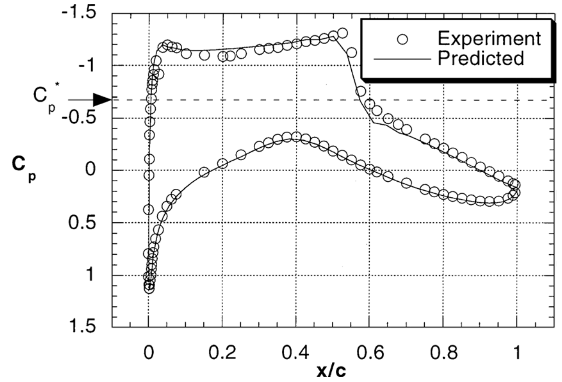

Fig. 11 Pressure distribution of RAE 2822 at $c_l = 0.80$, $M_\infty = 0.730$, and $Re = 6.5 \times 10^6$ (case 9).

Figure 12 depicts the total wake drag and its three components as a function of the integration station. The total drag is independent of the integration station except in the very near-wake region ($\Delta x/c < 0.25$). The contribution of the viscous-stress term never exceeds more than one drag count and becomes negligible at $\Delta x/c \approx 0.25$. The large pressure thrust term and the slightly larger momentum drag term nearly cancel each other in the near field and both terms decay with increasing distance until at $\Delta x/c \approx 10$, where the pressure term becomes negligible and the momentum term approaches its constant far-field value.

The results presented here were obtained for sufficiently fine meshes that grid convergence was attained. To prove this, the most challenging drag prediction problem, case 9, was solved with a finer grid with an increased number of mesh points (50% increase in both circumferential and normal directions from original grid). The last column of Table 2 lists the drag values based on the fine grid. The drag values are essentially the same as for the original grid, but the lift coefficient has increased very slightly because of improved shock resolution.

Table 3 Predicted drag decomposition for RAE 2822

Parameter	Case 1	Case 9
c_d (experimental)	0.0085	0.0168
c_d (surface integration)	0.0085	0.0166
c_d (wake integration)	0.0082	0.0162
c_d (wave drag)	0.00003	0.0053

Table 4 Inviscid wave drag results for RAE 2822 at $M_\infty = 0.730$ (case 9)

Parameter	Value
c_l	0.804
c_d (surface integration)	0.0048
c_d (wake integration)	0.0048
c_d (entropy integration, shock)	0.0049
c_d (entropy integration, wake)	0.0048

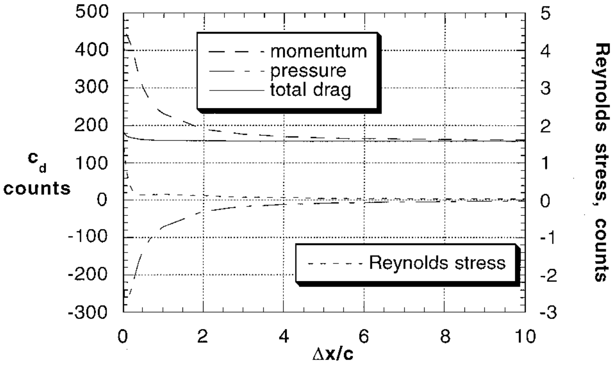

Fig. 12 Contribution of pressure, momentum-flux, and Reynolds stress terms to wake integral of RAE 2822 (case 9).

Wave drag calculations based on Eq. (11) are conducted for both RAE test cases. The greatest difficulty in predicting the wave drag from viscous flow solutions is setting the limits for the shock-contour integration. The reason for setting limits is to distinguish between entropy generated from shocks versus entropy generated from viscous effects that are due to the boundary layer. Near the boundary layer, viscous effects are large; thus an integration limit that encompasses even a small portion of the boundary layer may result in large changes to the wave drag value. The current procedure is to inspect the flowfield visually and deduce the limits of integration from examining the flowfield variables, especially near the edge of the boundary layer. Although this method seems to have produced reasonable values, further research will be needed to find a less subjective process.

The wave drag results are tabulated in Table 3 along with the total drag values repeated from the previous tables. For case 1 the wave drag is essentially negligible, an expected result as there is only a very weak shock present. Thus the total drag is basically completely due to viscous effects. For case 9 the wave drag is 53 counts and comprises approximately one-third of the total drag, i.e., the viscous drag is approximately 113 counts. This is in good agreement with the drag values obtained by Lock.[1]

To validate the wave drag prediction further, case 9 was analyzed based on an Euler solution. In addition to the surface integration, the wake integration, and the entropy integration across the shock, a fourth drag evaluation method was also included: integrating the entropy increase along a wake cut similar to the wake integration. In Table 4 the wave drag results based on an Euler solution for case 9 are presented. All four drag evaluation techniques provide nearly identical values, and the inviscid wave drag value is similar to the value obtained from the viscous solution. Slight differences are expected between the two wave drag values based on the fact that the viscous and the inviscid pressure distributions differ slightly as a result of the boundary-layer displacement effects.

Conclusions

The main objective of this paper is to compare the consistency of predicting the drag of airfoils in subsonic and transonic flows by use of body-surface integration and wake integration. Overall, wake integration shows potential as a simpler method than surface integration for calculating drag because no surface geometry is needed. Also, wake integration allows the decomposition of the total drag into its physical components, which is of importance to the prediction of scale effects on drag.

Results are presented for two airfoils and a range of Mach numbers: the NLF(1)-0416 at viscous low-subsonic flow conditions and the RAE 2822 at viscous and inviscid transonic flow conditions. Good agreement between predicted and measured drag values is obtained in all cases. Also, good agreement is obtained between predicted drag values based on surface integration and wake integration. The wave drag is derived separately from the entropy jump across the shocks. The wave drag estimation is validated by comparison against published results and by comparing results obtained with various drag prediction techniques for an inviscid transonic flow over the RAE 2822.

The next step is to combine the methodology described in this paper developed for drag prediction and decomposition of two-dimensional viscous flows with the previously published methodology for three-dimensional inviscid flows in order to provide a complete drag prediction and decomposition methodology for three-dimensional compressible viscous flows.

Acknowledgments

We thank Tom Pulliam and Stuart Rogers for their assistance and support and Dochan Kwak for providing the necessary CPU hours to conduct this study.

References

[1] Lock, R. C., "The Prediction of the Drag of Aerofoils and Wings at High Subsonic Speeds," *Aeronautical Journal*, Vol. 90, No. 896, 1986, pp. 207–226.

[2] Yu, N. J., Chen, H. C., Samant, S. S., and Rubbert, P. E., "Inviscid Drag Calculations for Transonic Flows," AIAA Paper 83-1928, July 1983.

[3] Slooff, J. W., "Computational Drag Analyses and Minimization: Mission Impossible?," *Drag Prediction and Minimization*, AGARD-R-723, Addendum I, AGARD, 1986.

[4] van der Vooren, J., and Slooff, J. W., "CFD Based Drag Prediction: State-of-the-Art Theory, Prospects," National Aerospace Lab., NLR TP 90247L, The Netherlands, Aug. 1990.

[5] Lock, R. C., "Prediction of the Drag of Wings at Subsonic Speeds by Viscous/Inviscid Interaction Techniques," *Drag Prediction and Minimization*, AGARD-R-723, AGARD, July 1985, pp. 10-1–10-71.

[6] van Dam, C. P., and Nikfetrat, K., "Accurate Prediction of Drag Using Euler Methods," *Journal of Aircraft*, Vol. 29, No. 3, 1992, pp. 516–519.

[7] van Dam, C. P., Nikfetrat, K., Wong, K., and Vijgen, P. M. H. W., "Drag Prediction at Subsonic and Transonic Speeds Using Euler Methods," *Journal of Aircraft*, Vol. 32, No. 4, 1995, pp. 839–845.

[8] Oswatitsch, K., "Der Luftwiderstand als Integral des Entropiestromes," *Nachrichten der Akadamie der Wissenschaften in Göttingen, Mathematisch-Physikalische Klasse*, Heft 1, 1945, pp. 88–90.

[9] Walatka, P. P., Buning, P. G., Pierce, L., and Elson, P. A., "PLOT3D User's Manual," NASA TM 101067, July 1992.

[10] Pulliam, T. H., and Steger, J. L., "Implicit Finite Difference Simulations of Three-Dimensional Compressible Flow," *AIAA Journal*, Vol. 18, No. 2, 1989, pp. 159–167.

[11] Rogers, S. E., and Kwak, D., "An Upwind Differencing Scheme for the Incompressible Navier-Stokes Equations," *Applied Numerical Mathematics*, Vol. 8, No. 1, 1991, pp. 43–64.

[12] Beam, R., and Warming, R. F., "An Implicit Finite-Difference Algorithm for Hyperbolic Systems in Conservation Law Form," *Journal of Computational Physics*, Vol. 22, No. 1, 1976, pp. 87–110.

[13] Barth, T. J., Pulliam, T. H., and Buning, P. G., "Navier-Stokes Computations for Exotic Airfoils," AIAA Paper 85-0109, Jan. 1985.

[14] Pulliam, T. H., "Efficient Solution Methods for the Navier-Stokes Equations," *Lecture Notes for the von Kármán Institute for Fluid Dynamics Lecture Series: Numerical Techniques for Viscous Flow Computation in Turbomachinery Bladings,* von Kármán Inst. for Fluid Dynamics, Rhode Saint Genèse, Belgium, Jan. 1986, pp. 1–137.

[15] Zingg, D. W., "Low Mach Number Euler Computations," *Canadian Aeronautics and Space Journal*, Vol. 36, No. 3, 1990, pp. 146–152.

[16] Chorin, A. J., "A Numerical Method for Solving Incompressible Viscous Flow Problems," *Journal of Computational Physics*, Vol. 2, No. 1, 1967, pp. 12–26.

[17] Roe, P. L., "Approximate Riemann Solvers, Parameter Vectors, and Difference Scheme," *Journal of Computational Physics*, Vol. 43, No. 2, 1981, pp. 357–372.

[18] Rogers, S. E., Wiltberger, N. L., and Kwak, D., "Efficient Simulation of Incompressible Viscous Flow over Single and Multielement Airfoils," *Journal of Aircraft*, Vol. 30, No. 5, 1993, pp. 736–743.

[19] Rogers, S. E., "Progress in High-Lift Aerodynamic Calculations," *Journal of Aircraft*, Vol. 31, No. 6, 1994, pp. 1244–1251.

[20] Cao, H. V., and Kusunose, K., "Grid Generation and Navier-Stokes Analysis for Multi-Element Airfoils," AIAA Paper 94-0748, Jan. 1994.

[21] Spalart, P. R., and Allmaras, S. R., "A One-Equation Turbulence Model for Aerodynamic Flows," AIAA Paper 92-0439, Jan. 1992.

[22] Chan, W. M., Chiu, I.-T., and Buning, P. G., "User's Manual for the HYPGEN Hyperbolic Grid Generator and the HGUI Graphical User Interface," NASA TM 108791, Oct. 1993.

[23] Somers, D. M., "Design and Experimental Results for a Natural-Laminar-Flow Airfoil for General Aviation Applications," NASA TP-1861, June 1981.

[24] Cook, P. H., McDonald, M. A., and Firmin, M. C. P., "Aerofoil RAE 2822—Pressure Distributions, and Boundary Layer and Wake Measurements," *Experimental Data Base for Computer Program Assessment*, AGARD-AR-138, AGARD, 1979, pp. A6-1–A6-77.